

Approaching quantum-limited cw anti-Stokes conversion through cavity-enhanced Raman-resonant four-wave mixing

P. A. Roos,^{*} L. S. Meng, S. K. Murphy, and J. L. Carlsten[†]

Department of Physics, Montana State University, Bozeman, Montana 59717

Abstract

Building on previous efficient Raman downconversion achievements, we present analytical theoretical results predicting that the upconversion efficiency from a continuous-wave pump beam into a single Raman anti-Stokes order can approach the quantum limit of 50%. We consider high-finesse cavity enhancement of the Raman-resonant four-wave mixing process to enable pumping with relatively low-power lasers. In addition to its practical value as a means of efficiently upconverting visible and near-infrared continuous-wave laser light, this technique can offer a probe into the fundamental limits and gain suppression subtleties associated with Raman-resonant four-wave mixing.

© 2003 Optical Society of America

OCIS codes: 190.4380, 190.7220.

^{*}Present address: JILA, National Institute of Standards and Technology, and University of Colorado, Boulder, Colorado 80309-0440

[†]Electronic address: carlsten@physics.montana.edu

1. INTRODUCTION

There has been a growing effort to improve the efficiency with which a pump beam can be frequency upconverted into an anti-Stokes beam through the Raman-resonant four-wave-mixing (FWM) process. In the pulsed laser regime, anti-Stokes conversion improvements have involved temporal pulse shaping, spatial focusing, and off-axis Stokes seeding.^{1,2} More recently, researchers have explored near-maximal atomic coherence techniques.³⁻⁵ However, little research has been performed in the lower-power continuous-wave (cw) regime, presumably due to insufficient gain for the nonlinear process.

We are aware of three previous studies for which cw anti-Stokes conversion is significant.⁶⁻⁸ Each of these utilizes a pump source whose frequency is nearly resonant with a single-photon transition in an atomic vapor. From the data shown by Gauthier, Malcuit, and Boyd,⁶ one can estimate the maximum anti-Stokes power conversion efficiency to be near 3%, while Zibrov, Lukin, and Scully⁸ report a maximum power conversion of 4% into multiple orders of Stokes and anti-Stokes combined. No cavity enhancement was needed for these studies because of the enhanced nonlinearity near the single-photon resonances. However, for the purpose of optical frequency conversion, reliance on these atomic resonances has the adverse effect of severely limiting the suitable pump source frequencies, and therefore the generated optical frequencies. In the present work, we describe theoretically how it is possible to approach the quantum conversion limit of 50% from a cw pump laser into a single anti-Stokes order using high-finesse cavity (HFC) enhancement of the Raman-resonant FWM process in diatomic hydrogen gas. All of the optical frequencies involved are very far detuned from any single-photon atomic transitions, which permits frequency upconversion of laser sources throughout the visible and near-infrared spectral regions.

Similar HFC enhancement techniques were recently exploited to efficiently *downconvert*

low-power cw pump laser light into Stokes light by placing gaseous Raman media (H_2 or D_2) within doubly-resonant HFCs.^{9,10} For these Raman systems, researchers have experimentally demonstrated input threshold powers of under 1 mW,¹¹ output linewidths below 10 kHz,⁹ output optical powers exceeding 160 mW,¹⁰ and photon conversions approaching 70%.¹² Photon conversions are predicted to approach the quantum limit of 100% with properly chosen mirrors.¹³ Researchers have accurately modeled the output behavior of these systems by approximating the hydrogenic molecules as three-level Λ systems interacting with the cavity-enhanced pump and Stokes field modes.^{9,14,15} A very small amount of parametric anti-Stokes light accompanied the Stokes emission from these cw Raman systems.¹⁶ This emission was treated theoretically with the assumption that the anti-Stokes generation did not appreciably affect the other two fields because there was no anti-Stokes cavity enhancement in these systems. In another related work, Shinzen and co-workers numerically studied the possibility of using HFC enhancement of the anti-Stokes field to generate highly repetitive optical pulses.¹⁷ In the present work, we demonstrate how the HFC enhancement techniques used for cw Raman downconversion can be used for efficient cw anti-Stokes upconversion via the Raman-resonant FWM process.

After this introduction, we use Section 2 to outline the derivation for the time-dependent intracavity field equations for this system. In Section 3 we derive and discuss analytical steady-state expressions for the intracavity optical powers, the Stokes laser threshold, and the photon conversion efficiencies. In Section 4 we discuss the challenges and possibilities of experimentally realizing this cw anti-Stokes generation system. In the final section, we review our findings and provide some concluding thoughts.

2. TIME-DEPENDENT RESULTS

Throughout this work, we consider the $S_{00}(1)$ rotational Raman transition (shift= 587 $\text{cm}^{-1} = 17.6$ THz) in diatomic hydrogen gas as a specific example.¹⁸ We assume that the Raman gas occupies the volume between the mirrors of a HFC, as has been previously demonstrated. We approximate the hydrogen molecules as three-level systems as shown in Fig. 1(a). Level 1 represents the ground state, level 2 the first excited rotational state, and level 3 the first excited electronic state of the molecule. Single-photon 1–2 transitions are forbidden by selection rules.

During the anti-Stokes generation process, the Raman medium interacts with three strongly cavity-enhanced fields: the input pump (ω_p), the generated Stokes (ω_s), and the generated anti-Stokes (ω_{as}). We consider the case where the input pump laser is in the visible (532 nm) spectral region, so that the three optical fields are all very far detuned [by $\Delta = 63,170 \text{ cm}^{-1} = 1,895$ THz and $\Delta_{as} = 62,580 \text{ cm}^{-1} = 1,877$ THz in Fig. 1(a)] from the allowed single-photon transitions (1–3 and 2–3). In Fig. 1(a), we identify two Raman interactions that are involved with the anti-Stokes generation: “Raman 1” for the pump \leftrightarrow Stokes interaction, and “Raman 2” for the anti-Stokes \leftrightarrow pump interaction. The FWM interaction involves all the fields. The presence of level 2 allows all these interactions to be Raman (two-photon) resonant ($\omega_p - \omega_s = \omega_{as} - \omega_p = \omega_2 - \omega_1$).

There are several ways to obtain the semiclassical time-dependent field equations for this system. One can use the work of Harris and Sokolov¹⁹ in the appropriate limits and modified to accommodate cavity enhancement.¹⁵ Alternatively it is possible to apply the Heisenberg equation of motion directly to the Hamiltonian that describes the interactions shown in Fig. 1(a).²⁰ In either case, one can use the fact that the single-photon detunings are by far the largest rates in the system (including the Rabi frequencies) to adiabatically eliminate

the atomic coherences that involve level 3, disregard single-photon absorption, ignore the level 3 population, and neglect Stark shifts and power broadening. Furthermore, one can also adiabatically eliminate the Raman (1–2) coherence and neglect population in level 2 for the decay rates and optical powers that are appropriate to this system. With these simplifications we derive the following coupled intracavity field equations²⁰

$$\dot{\alpha}_p = -\kappa_p \alpha_p - G_1 |\alpha_s|^2 \alpha_p + G_2 |\alpha_{as}|^2 \alpha_p + \tau_{\text{rt}}^{-1} \sqrt{T_{p,0}} \alpha_p^{\text{in}}, \quad (1)$$

$$\dot{\alpha}_s = -\kappa_s \alpha_s + G_1 |\alpha_p|^2 \alpha_s + G_{12} \alpha_p^2 \alpha_s^*, \quad (2)$$

$$\dot{\alpha}_{as} = -\kappa_{as} \alpha_{as} - G_2 |\alpha_p|^2 \alpha_{as} - G_{12} \alpha_p^2 \alpha_s^*, \quad (3)$$

where the α 's are unitless complex intracavity field amplitudes, except for α_p^{in} , which is the external input pump field, τ_{rt} is the cavity round-trip time, κ 's are cavity field decay rates [$\kappa \equiv -(\ln R_{\text{rt}})/2\tau_{\text{rt}}$ where R_{rt} is the round-trip power reflectivity], $T_{p,0}$ is the power transmissivity of the input coupler mirror at the pump wavelength, and the G 's are gains; G_1 for the pump \leftrightarrow Stokes Raman interaction (Raman 1), G_2 for the anti-Stokes \leftrightarrow pump Raman interaction (Raman 2) and G_{12} for the FWM interaction. Because we assume Raman resonance, G_1 and G_2 are real, but G_{12} can still be complex.

In Eqs. (1) - (3) we have assumed that all three fields are resonant with *active* modes of the HFC. This is justified for the pump field because its frequency can be electronically stabilized to an active cavity mode, and for the Stokes field because it will build on the active cavity mode nearest to the Raman gain linecenter. However, this is only justified for the anti-Stokes field when the Raman gas dispersion can be compensated for each round trip in the cavity. Experimentally achieving this condition will be discussed in Section 4. Even though we assume that the mode pulling effects of the Raman gas dispersion can be compensated, we still must account for the phase mismatch effects of the Raman gas

dispersion over one round trip. These effects are included in the calculation of the FWM gain, G_{12} . Specifically, we incorporate the Boyd-Kleinman factors²¹ in the analysis and find that each of the G 's involves a spatial overlap integral over the cavity modes associated with the particular process. We will soon show that the integral in G_{12} generates the deleterious phase-mismatch parameter that is due to the dispersion of the gas molecules.

It is worth noting here that no FWM terms (those with G_{12}) directly influence the pump field dynamics in Eq. (1). Furthermore, from the equations for the lower level populations (which don't appreciably affect the fields),²⁰

$$\begin{aligned} \dot{J}_{11} = & \bar{\gamma}_{21} J_{22} - 2 G_1 |\alpha_s|^2 |\alpha_p|^2 - 2 G_2 |\alpha_p|^2 |\alpha_{as}|^2 \\ & - [2 G_{12} \alpha_p^2 \alpha_s^* \alpha_{as}^* + \text{c.c.}], \end{aligned} \quad (4)$$

$$\dot{J}_{22} = - \dot{J}_{11}, \quad (5)$$

where $\bar{\gamma}_{21}$ is the population decay rate of level 2, one can see that there *are* FWM contributions to the populations of levels 1 and 2. This evidence supports the assertion by Bobbs and Warner that the FWM interaction involves energy exchange with the medium.²² Therefore, the more detailed energy level diagram given in Fig. 1(b), which shows the direction of energy flow, does not correctly describe the FWM contributions alone. However, we will soon show that when all interactions (FWM *and* Raman) are included, one can correctly interpret the overall anti-Stokes generation process as involving no net energy exchange with the medium as shown in Fig. 1(b).

3. STEADY-STATE RESULTS

By setting Eqs. (1) - (3) to zero, and after a fair amount of algebraic manipulation, the steady-state unitless semiclassical intracavity powers above threshold can be expressed as

$$|\alpha_p|^2 = \left(\frac{1}{1-x} \right) \frac{\kappa_s}{G_1}, \quad (6)$$

$$|\alpha_s|^2 = \left(\frac{1}{1-x^2/y} \right) \frac{\kappa_p}{G_1} (\sqrt{r_p} - 1), \quad (7)$$

$$|\alpha_{as}|^2 = \left(\frac{x-x^2/y}{1-x} \right) \frac{\kappa_s}{\kappa_{as}} |\alpha_s|^2, \quad (8)$$

where $r_p \equiv |\alpha_p^{\text{in}}|^2 / |\alpha_p^{\text{th}}|^2$ is the incident unitless pump power normalized to threshold, which is given by

$$|\alpha_p^{\text{th}}|^2 = \left(\frac{1}{1-x} \right) \frac{\kappa_p^2 \kappa_s \tau_{\text{rt}}^2}{G_1 T_{p,0}}. \quad (9)$$

In the above expressions, the unitless quantity

$$x \equiv \begin{cases} 1 - \frac{2x_0(1-y)}{[(1-x_0)^2 + 4x_0(1-y)]^{1/2} - (1-x_0)} & (0 < y < 1) \\ x_0. & (y = 1) \end{cases} \quad (10)$$

depends on the two unitless parameters y and x_0 . We find that y depends only on the spatial overlaps of the three active cavity modes and is given by

$$y \equiv \frac{|G_{12}|^2}{G_1 G_2} = \frac{\left| \int_{atoms} u_p^2 u_s^* u_{as}^* d\mathbf{r} \right|^2}{\left(\int_{atoms} |u_p|^2 |u_s|^2 d\mathbf{r} \right) \left(\int_{atoms} |u_{as}|^2 |u_p|^2 d\mathbf{r} \right)}, \quad (11)$$

where the integrals are over the volume containing the atoms and the u 's are the active cavity eigenmodes. Physically, y is a measure of how well the cavity modes overlap spatially for the purpose of anti-Stokes generation. The numerator comes from the FWM contribution and includes the deleterious effects of the phase mismatch due to dispersion of the gas molecules. When the three cavity modes are identical (which can't happen unless the wavelengths are

identical), y reaches its maximum value of unity. Under more realistic circumstances, the three active cavity modes don't perfectly overlap in space due to disparate waist sizes and standing wave periods (if a standing wave cavity is used), and due to dispersion-induced phase mismatch in the Raman gas. These factors reduce y below unity.

Assuming traveling-wave fundamental Gaussian cavity modes in the plane-wave limit (when the confocal parameter is greater than the cavity length), the previous expression can be simplified to

$$y \approx \frac{4(k_p + k_s)(k_{as} + k_p)}{(2k_p + k_s + k_{as})^2} \operatorname{sinc} \left[\frac{L}{2}(2k_p - k_s - k_{as}) \right], \quad \left(\begin{array}{l} \text{traveling waves,} \\ \text{plane-wave limit} \end{array} \right) \quad (12)$$

where the k 's are wavenumbers for the various fields in the gas. The initial fraction is a measure of the spatial overlap in the radial dimension, while the sinc function accounts for the phase mismatch in the axial dimension. For the rotational H₂ Raman shift under consideration at a pressure of 8 atm, a temperature of 295 K, and for a 30-cm round-trip cavity length, $y = 0.972$. The refractive indices needed for this calculation were extrapolated from a polynomial fit to existing experimental data at other wavelengths.²³ For systems with larger Raman shifts, longer cavity lengths, or higher pressures, the y parameter will be smaller.

The important parameter x_0 in Eq. (10) depends on the relative strengths of the cavity-enhanced Raman processes involved rather than on the spatial aspects of the cavity, and is given by

$$x_0 \equiv \frac{G_2}{G_1} \frac{\kappa_s}{\kappa_{as}} \approx \frac{G_2 \mathcal{F}_{as}}{G_1 \mathcal{F}_s}, \quad (13)$$

where \mathcal{F}_{as} and \mathcal{F}_s are the cavity finesses at the anti-Stokes and Stokes wavelengths, respectively. The parameter x_0 can therefore be interpreted physically as the relative effective gain

for the two cavity-enhanced Raman processes present in this system. Experimentally, one can adjust x_0 by changing the relative reflectivities of the cavity mirrors at the Stokes and anti-Stokes wavelengths. When the cavity-enhanced Raman gains are equal, $x_0 = 1$.

There are two important aspects of Eqs. (6) - (9) that deserve discussion. First, when $x_0 \ll 1$, corresponding to no anti-Stokes cavity enhancement, $x \rightarrow 0$ regardless of y and the equations directly match the theoretical and experimental behavior of the strictly Stokes generation systems that have been previously achieved for frequency downconversion.^{9,20} Even with the anti-Stokes enhancement, the behavior is still very similar to that of the strictly Stokes generation systems: the pump power above threshold is independent of the pump rate (it simply clamps at a higher level) and the Stokes power grows as the square root of the pump rate (a portion is simply diverted to anti-Stokes). Second, as x approaches unity, which occurs for excellent spatial overlap and phase matching ($y \rightarrow 1$) and when the two cavity-enhanced Raman gains are nearly equal ($x_0 \rightarrow 1$), the Stokes laser threshold from Eq. (9) increases dramatically. We interpret this threshold rise as a direct manifestation of a Raman gain suppression phenomenon that was predicted by Bloembergen and Shen long ago²⁴ and later observed experimentally by several groups in the pulsed laser regime.^{25,26} It is also possible to view the gain suppression as quantum interference between the two Raman pathways to level 2.

Although enhancement of the anti-Stokes field can therefore suppress the Stokes gain, we find that this gain suppression is also directly associated with an increased photon conversion to the anti-Stokes. To see this, we convert the intracavity optical powers given by Eqs. (7) and (8) into powers exiting the cavity. It is then straightforward to show that the peak conversion efficiency for both the Stokes and the anti-Stokes occurs for a pump rate of four times the Stokes laser threshold ($r_p = 4$), as for the strictly Stokes generation systems.¹³ At

this pump rate, the peak conversion efficiencies are given by

$$\eta_s = \frac{|\alpha_s^{\text{out}}|^2}{4|\alpha_p^{\text{th}}|^2} = \left(\frac{1-x}{1-x^2/y} \right) \frac{T_{p,0}}{(1-R_{p,\text{rt}})} \frac{T_{s,0}}{(1-R_{s,\text{rt}})} \quad (14)$$

$$\eta_{as} = \frac{|\alpha_{as}^{\text{out}}|^2}{4|\alpha_p^{\text{th}}|^2} = \left(\frac{x-x^2/y}{1-x^2/y} \right) \frac{T_{p,0}}{(1-R_{p,\text{rt}})} \frac{T_{as,0}}{(1-R_{as,\text{rt}})}. \quad (15)$$

The photon conversion efficiencies, with the peak values given by Eqs. (14) and (15), are plotted in Fig. 2 as functions of the pump rate for several different values of the relative gain parameter x_0 . For these plots, we have assumed $y = 1$ (so that $x = x_0$) and that the input/output coupler transmission dominates the other cavity mirror losses [$T_0 \approx (1 - R_{\text{rt}})$]. All of the curves peak at a pump rate of $r_p = 4$, as expected. As the parameter x_0 is increased from zero to near unity, the peak Stokes conversion falls from 100% to 50%, while the peak anti-Stokes conversion grows from zero to 50%. Therefore, for excellent spatial overlap and phase matching ($y \rightarrow 1$), and when the cavity-enhanced gains for the two Raman processes are nearly equal ($x_0 \rightarrow 1$), the conversion efficiency approaches the quantum limit for anti-Stokes generation via the Raman-resonant FWM process. That is, a pair of pump photons is exchanged for one Stokes photon and one anti-Stokes photon, as shown in Fig. 1(b).

4. SYSTEM ANALYSIS

Clearly, imperfect spatial overlap and phase matching, as well as mirror losses will reduce the peak conversion efficiencies through Eqs. (14) and (15) for any experiment. However, a less explicit experimental obstacle is caused by the x dependence in Eq. (9). Although Fig. 2(b) illustrates that a value of x approaching unity is desirable for high conversion to anti-Stokes, this limit also corresponds to a prohibitive increase in the Stokes laser threshold due to gain suppression, making it more difficult to achieve the four-times-threshold condition required for optimal conversion.

To elucidate the relationship between the rising threshold and the increasing conversion,

Figs. 3(a) and 3(b) show the Stokes threshold from Eq. (9) and the peak anti-Stokes conversion efficiency from Eq. (15), both as functions of the experimentally accessible parameter x_0 . The horizontal axis can be viewed as a measure of the anti-Stokes cavity enhancement. We normalize the threshold curves in Fig. 3(a) to the case when $x_0 = 0$ (no anti-Stokes enhancement). The solid curves labeled A represent the ideal case of perfect spatial overlap, perfect phase matching, and impedance-matched lossless mirrors. Complete Stokes gain suppression occurs for this case when $x_0 = 1$ (equal cavity-enhanced gains for the two Raman processes). But despite the prohibitive threshold increase as x_0 approaches unity, substantial conversion can still be achieved for slightly lower values of x_0 , corresponding to very mild threshold increases. For instance, when $x_0 = 0.5$, the threshold only doubles relative to that when $x_0 = 0$, and the conversion efficiency reaches 33%. We find it interesting that the Stokes gain suppression was traditionally avoided in the production of anti-Stokes in the past, whereas it can now be interpreted as actually providing the *means* for anti-Stokes conversion in this system.

More realistic cases are given by the dotted curves labeled B and C in Figs. 3(a) and 3(b). The curves labeled B include the effects of imperfect spatial overlap and phase matching ($y = 0.972$), while the curves labeled C additionally include the effects of imperfect mirrors. For curves C, we assume that three of the four ring cavity mirrors are coated as highly reflective as currently possible [<10 parts per million (ppm) overall loss]. We assume that the final input/output coupler mirror exhibits 440 ppm transmission and 60 ppm absorption/scattering for all three wavelengths. The reason for the relatively high absorption will be discussed shortly. The imperfect phase matching prevents complete gain suppression from ever occurring for curves B and C, but the peak conversion still occurs for $x_0 = 1$. In the absence of anti-Stokes enhancement ($x_0 \approx 0$), the Stokes laser threshold is under

2 mW. With the nearly 10-fold increase in the laser threshold that is due to anti-Stokes enhancement at $x_0 = 1$ and mirror losses, anti-Stokes conversion can exceed 30% (occurring at four times threshold) with around 80 mW of injected pump light. The luxury of greater available pump power can afford conversion efficiencies approaching the fundamental limit of 50% by reducing the cavity length and increasing the input/output coupler transmissivity relative to the other cavity losses.

Up to this point, the effect of the Raman gas dispersion has been only to cause a phase mismatch (embedded in the y parameter) that limits the peak anti-Stokes generation by disrupting the quantum interference between the Stokes and anti-Stokes Raman channels. However, the Raman gas dispersion also complicates the formidable experimental challenge of ensuring that all three fields simultaneously resonate within the HFC. The conceptual schematic in Fig. 4 illustrates this problem (the schematic is not to scale). The longitudinal modes of the HFC (shown as dotted vertical lines) are not evenly distributed in frequency due to the gas dispersion. The pump laser is phase/frequency stabilized to one mode of the HFC and the Stokes field builds on the cavity mode nearest to its gain peak, as previously demonstrated.²⁷ However, dispersion of the hydrogen gas will prevent the generated anti-Stokes frequency ($\omega_{as} \equiv 2\omega_p - \omega_s$) from automatically matching a cavity resonance (by ~ 100 MHz for the system at hand). We therefore require that the input/output coupler compensate for this dispersion each round trip. Fortunately, such dispersion-compensated or “chirped” mirrors have recently received attention due to their roll in the generation of mode-locked femtosecond laser pulses.²⁸ The 60 ppm absorption of the input/output coupler used in the calculations above are conservative estimates from our experience with mirrors coated separately for two disparate wavelengths,¹² but are a bit lower than other chirped-mirror loss estimates.²⁸ The gas pressure, cavity reflection angle, and two-photon dispersion

can be used to fine tune the dispersion compensation and therefore to coerce the anti-Stokes field into resonance.

Other possibilities exist for achieving the triple-resonance condition without using a chirped input/output coupler. These include resonating the anti-Stokes in an adjacent longitudinal HFC mode or utilizing a higher order spatial mode to resonate one of the three fields. Unfortunately, these methods suffer from either decreased phase matching over the round-trip length or poorer spatial overlap of the active cavity modes. Nevertheless, the use of higher order spatial modes may provide an excellent opportunity to study the physical effects predicted in this work. In this case, the cavity geometry can be engineered such that a higher-order spatial mode resonance overlaps with the anti-Stokes generation frequency. Although the spatial overlap of the modes would not be optimal, this option would represent a valid experimental verification of the theory presented here and would avert the monetary and technical difficulties associated with manufacturing the chirped mirror. We also note here that the cavity-enhanced anti-Stokes emission will exhibit a high-quality spatial mode and a linewidth similar to that of the pump and Stokes fields (<10 kHz).⁹

5. CONCLUSION

In this work, we derived analytical results that predict the possibility of efficient cw anti-Stokes generation using cavity-enhanced Raman-resonant FWM. Our approach originated from previous successful experimental and theoretical research conducted on strictly Stokes (no anti-Stokes) generation systems. We attributed the predicted Stokes laser threshold rise with anti-Stokes cavity enhancement to a gain suppression phenomenon that was previously studied in the pulsed regime. This phenomenon can also be interpreted as quantum interference between the two Raman pathways present in the system. We identified poor spatial cavity mode overlap and phase matching, and mirror losses as the significant sources for de-

creased photon conversion efficiency from the fundamental quantum limit of 50%. However, we also identified the threshold rise and the need for dispersion compensation as significant, but surmountable challenges for experimental realization. Using a rotational Raman transition in diatomic hydrogen gas, we predicted that photon conversion can exceed 30% in a high-quality spatial mode for an input pump power of 80 mW.

Other transitions in other gases may ultimately prove more useful from a practical standpoint. For instance, a system that uses a frequency-doubled Nd:Yag pump source to drive the vibrational transition in diatomic deuterium gas is attractive as a simultaneous generator of red (Stokes = 633 nm), blue (anti-Stokes = 459 nm), and green (pump = 532 nm) for color projection systems. In addition to possible cw frequency upconversion applications, this technique can offer a probe into the fundamental limits and gain suppression subtleties of Raman-resonant FWM. The authors gratefully acknowledge Jason Brasseur for many useful discussions. This material is based upon work supported by the National Science Foundation under Grant No. 0097222.

References

1. C. Reiser, T. D. Raymond, R. B. Michie, and A. P. Hickman, “Efficient anti-Stokes Raman conversion in collimated beams,” *J. Opt. Soc. Am. B*, **6**, 1859-1869 (1989).
2. M. Suzuki, S. Wada, and H. Tashiro, “Temporally resolved ring-shaped patterns beyond the phase-matching angle in the Stokes and anti-Stokes waves,” *J. Opt. Soc. Am. B*, **14**, 1672-1679 (1997).
3. M. Jain, H. Xia, G. Y. Yin, A. J. Merriam, and S. E. Harris, “Efficient nonlinear frequency conversion with maximal atomic coherence,” *Phys. Rev. Lett.*, **77**, 4326-4329 (1996).
4. A. J. Merriam, S. J. Sharpe, H. Xia, D. Manuszak, G. Y. Yin, and S. E. Harris, “Efficient gas-phase generation of coherent vacuum ultraviolet radiation,” *Opt. Lett.*, **24**, 625-627 (1999).
5. D. D. Yavuz, D. R. Walker, G. Y. Yin, and S. E. Harris, “Rotational Raman generation with near-unity conversion efficiency,” *Opt. Lett.*, **27**, 769-771 (2002).
6. D. J. Gauthier, M. S. Malcuit, and R. W. Boyd, “Polarization instabilities of counter-propagating laser beams in sodium vapor,” *Phys. Rev. Lett.*, **61**, 1827-1830 (1988).
7. D. J. Gauthier, M. S. Malcuit, A. L. Gaeta, and R. W. Boyd, “Polarization bistability of counterpropagating laser beams,” *Phys. Rev. Lett.*, **64**, 1721-1724 (1990).
8. A. S. Zibrov, M. D. Lukin, and M. O. Scully, “Nondegenerate parametric self-oscillation via multiwave mixing in coherent atomic media,” *Phys. Rev. Lett.*, **83**, 4049-4052 (1999).
9. J. K. Brasseur, P. A. Roos, K. S. Repasky, and J. L. Carlsten, “Characterization of a continuous-wave Raman laser in H₂,” *J. Opt. Soc. Am. B*, **16**, 1305-1312 (1999).
10. J. K. Brasseur, R. F. Teehan, P. A. Roos, and J. L. Carlsten, “High power deuterium

- Raman laser at 532 nm,” Submitted to Appl. Opt., (2003).
11. P. A. Roos, J. K. Brasseur, and J. L. Carlsten, “Diode-pumped nonresonant continuous-wave Raman laser in H₂ with resonant optical feedback stabilization,” Opt. Lett., **24**, 1130-1132 (1999).
 12. L. S. Meng, P. A. Roos, K. S. Repasky, and J. L. Carlsten, “High-conversion-efficiency, diode-pumped continuous-wave Raman laser,” Opt. Lett., **26**, 426-428 (2001).
 13. K. S. Repasky, J. K. Brasseur, L. S. Meng, and J. L. Carlsten, “High-efficiency, continuous-wave Raman lasers,” J. Opt. Soc. Am. B, **16**, 717-721 (1999).
 14. P. A. Roos, S. K. Murphy, L. S. Meng, J. L. Carlsten, T. C. Ralph, A. G. White, and J. K. Brasseur, “Quantum theory of the far-off-resonance cw Raman laser: Heisenberg-Langevin approach,” Phys. Rev. A, **68**, 013802/1-12 (2003).
 15. L. S. Meng, “Continuous-wave Raman laser in H₂: semiclassical theory and diode pumping experiments,” Ph.D. Thesis, Department of Physics, Montana State University, September, 2002, www.physics.montana.edu/optics/jlc/phd.html.
 16. J. K. Brasseur, P. A. Roos, and J. L. Carlsten, “Coherent anti-Stokes emission in a continuous-wave Raman laser in H₂,” J. Opt. Soc. Am. B, **17**, 1223-1228 (2000).
 17. K. Shinzen, Y. Hirakawa, and T. Imasaka, “Generation of highly repetitive optical pulses based on intracavity four-wave Raman mixing,” Phys. Rev. Lett., **87**, 223901/1-4 (2001).
 18. L. S. Meng, P. A. Roos, and J. L. Carlsten, “Continuous-wave rotational Raman laser in H₂,” Opt. Lett., **27**, 1226-1228 (2002).
 19. S. E. Harris and A. V. Sokolov, “Broadband spectral generation with refractive index control,” Phys. Rev. A, **55**, R4019-4022 (1997).
 20. P. A. Roos, “The diode-pumped continuous-wave Raman laser: Classical, quantum,

- and thermo-optic fundamentals,” Ph.D. Thesis, Department of Physics, Montana State University, October, 2002, www.physics.montana.edu/optics/jlc/phd.html.
21. G. D. Boyd and D. A. Kleinman, “Parametric interaction of focused Gaussian light beams,” *J. Appl. Phys.*, **39**, 3597-3639 (1968).
 22. B. Bobbs and C. Warner, “Raman-resonant four-wave mixing and energy transfer,” *J. Opt. Soc. Am. B*, **7**, 234-238 (1990).
 23. D. E. Gray (ed.), “American Institute of Physics Handbook,” 2nd. Ed., 6-95 (McGraw Hill, 1963).
 24. N. Bloembergen and Y. R. Shen, “Coupling between vibrations and light waves in Raman laser media,” *Phys. Rev. Lett.*, **12**, 504-507 (1964).
 25. G. V. Venkin, Yu. A. Il’inskii, and G. M. Mikheev, “Influence of the polarization of radiation on the energy characteristics and threshold of stimulated Raman scattering due to rotational transitions,” *Sov. J. Quantum Electron.*, **12**, 395-397 (1985).
 26. M. D. Duncan, R. Mahon, J. Reintjes, and L. L. Tankersley, “Parametric Raman gain suppression in D₂ and H₂,” *Opt. Lett.*, **11**, 803-805 (1986).
 27. J. K. Brasseur, P. A. Roos, L. S. Meng, and J. L. Carlsten, “Frequency tuning characteristics of a continuous-wave Raman laser in H₂,” *J. Opt. Soc. Am. B*, **17**, 1229-1232 (2000).
 28. K. Gabel, P. Rubbuldt, R. Lebert, P. Loosen, R. Poprawe, and H. Heyer, “Diode pumped, chirped mirror compensated, fs-laser,” *Opt. Commun.*, **153**, 275-281 (1998).

List of Figure Captions

Fig. 1. To-scale energy level diagram showing (a) the pertinent atomic levels, fields, and single-photon detunings (Δ 's), and (b) the energy flow for the overall anti-Stokes generation process.

Fig. 2. Photon conversion efficiencies for (a) the Stokes and (b) the anti-Stokes as functions of the pump rate. Curves are given for several different values of the relative gain parameter x_0 , and for idealized experimental conditions. The peak conversion occurs for $r_p = 4$.

Fig. 3. Plots showing (a) the normalized laser threshold and (b) the anti-Stokes photon conversion efficiency as functions of the relative gain parameter x . The solid curves represent idealized conditions, the dotted curves labeled B include imperfect spatial overlap and phase matching, and the dotted curves labeled C additionally include mirror losses.

Fig. 4. Conceptual schematic showing high-finesse cavity longitudinal modes in the presence of dispersion. Vertical lines represent longitudinal cavity modes. The pump laser frequency is actively stabilized to one cavity mode resonance (ω_p) and the Stokes builds automatically on another (ω_s). However, the anti-Stokes generation frequency (ω_{as}) does not match a cavity mode resonance frequency unless dispersion compensation measures are taken.

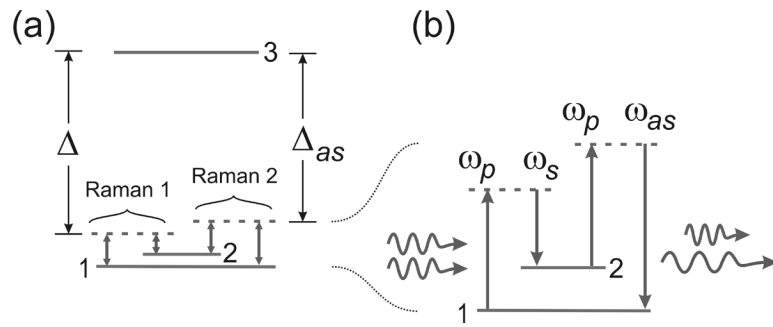


Fig. 1. To-scale energy level diagram showing (a) the pertinent atomic levels, fields, and single-photon detunings (Δ 's), and (b) the energy flow for the overall anti-Stokes generation process.

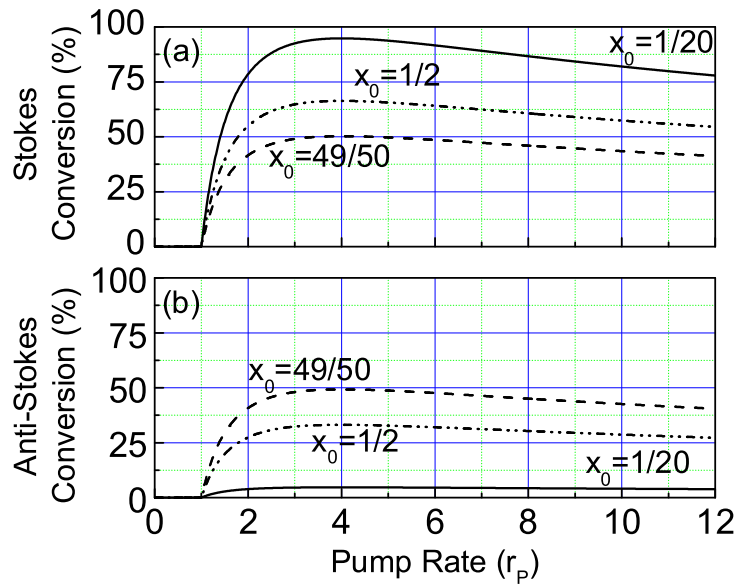


Fig. 2. Photon conversion efficiencies for (a) the Stokes and (b) the anti-Stokes as functions of the pump rate. Curves are given for several different values of the relative gain parameter x_0 , and for idealized experimental conditions. The peak conversion always occurs for $r_p = 4$.

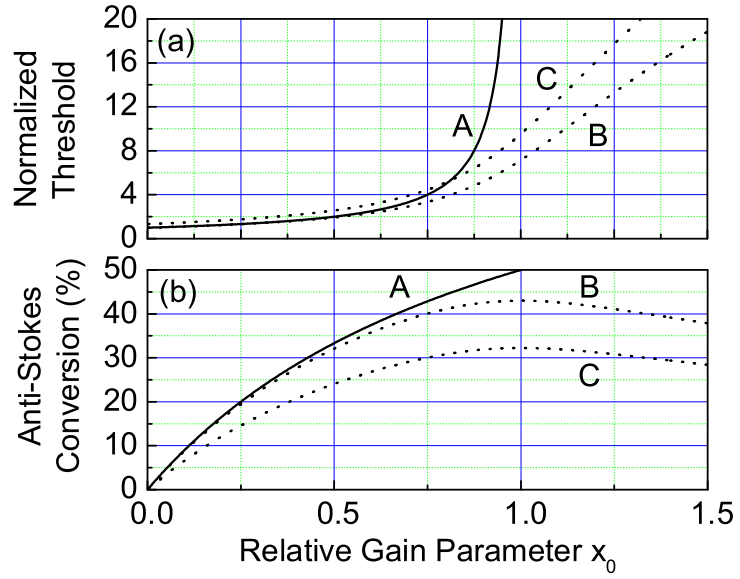


Fig. 3. Plots showing (a) the normalized laser threshold and (b) the anti-Stokes photon conversion efficiency as functions of the relative gain parameter x_0 . The solid curves represent idealized conditions, the dotted curves labeled B include imperfect spatial overlap and phase matching, and the dotted curves labeled C additionally include mirror losses.

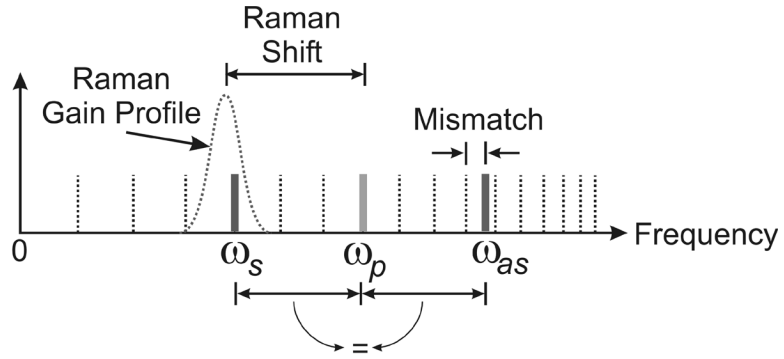


Fig. 4. Conceptual schematic showing high-finesse cavity longitudinal modes in the presence of dispersion due to the Raman gas. Vertical lines represent longitudinal cavity modes. The pump laser frequency is actively stabilized to one cavity mode resonance (ω_p) and the Stokes builds automatically on another (ω_s). However, the anti-Stokes generation frequency (ω_{as}) does not match a cavity mode resonance frequency unless dispersion compensation measures are taken.